

## Constructing Ordered Ion Transport Channel in Anion Exchange Membranes by Coordination Induction of Cu<sup>2+</sup> Ions

Caili Yuan, Yuhang Chen, Xiaoqin Ma, Xiaoli Lu, Wei Yuan, Jianchuan Wang,\* and Zidong Wei\*



Cite This: *Macromolecules* 2025, 58, 4206–4214



Read Online

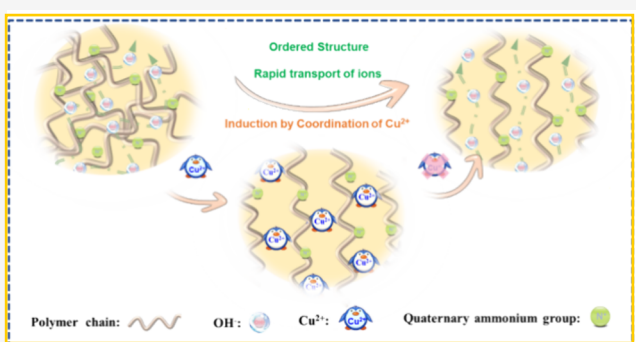
ACCESS |

Metrics & More

Article Recommendations

Supporting Information

**ABSTRACT:** Promising anion exchange membranes (AEMs) are increasingly utilized for ion transport in various electrochemical devices operating under alkaline conditions. Achieving efficient hydroxide transport is essential for superior electrochemical performance. Herein, we propose a novel method to construct ordered ion transport channels in AEMs by coordination induction. The coordination of Cu<sup>2+</sup> ions with diazafluorene induces an ordered structure of the polymer chain segments within the AEMs, thereby forming an ordered channel for fast ion transport in the membrane after the removal of Cu<sup>2+</sup> ions. The fabricated AEMs exhibit ion channel size between 2.82 and 3.43 nm. Compared to the AEMs without coordination induction, the OH<sup>-</sup> conductivity of the as-prepared AEMs was enhanced by approximately 4.7 times at most. Furthermore, the AEMs with ordered ion channel demonstrate impressive performance in both AEMFCs and AEMWEs, achieving a peak power density of 1.2 W cm<sup>-2</sup> and a current density of 3.4 A cm<sup>-2</sup>, respectively.



### INTRODUCTION

Anion exchange membranes (AEMs), composed of a polymer matrix embedded with positively charged functional groups, are primarily employed for ion transport in various fields, including anion exchange membrane fuel cells (AEMFCs) and anion exchange membrane water electrolyzers (AEMWEs).<sup>1–3</sup> Unlike proton exchange membranes (PEMs), AEMs offer the advantage of compatibility with nonprecious metal catalysts, leading to substantial cost reductions.<sup>4–6</sup> The performance of AEMs is crucial for the efficiency of hydrogen energy conversion devices; yet, they face challenges such as low ionic conductivity and insufficient alkaline stability, impeding their widespread use.

In order to address these challenges and develop high-performance AEM materials, extensive research has been conducted to synthesize polymers with improved OH<sup>-</sup> conductivity. Drawing inspiration from the Nafion membrane developed by DuPont, it is well-established that the construction of ion transport channels is an effective strategy for enhancing conductivity. To date, researchers have investigated various approaches for constructing these ion transport channels. For example, a Nafion membrane-like idea was used to introduce hydrophilic and hydrophobic phases into the AEM chain segments, utilizing the incompatibility of the two phases to form a microphase separation structure. The notable hydrophilicity difference between the olefinic backbone and the quaternary ammonium group renders poly(olefin)-based AEMs prone to microphase-separated structures, leading to enhanced ion transport rates and even a direct one-fold increase in OH<sup>-</sup> conductivity.<sup>7</sup> Additionally, the synergistic interaction of cations

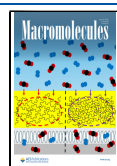
and highly hydrophobic fluorinated side chains further promotes enhanced microphase separation structures,<sup>8,9</sup> resulting in the creation of ionic transport channels in poly aryl AEMs and leading to an increase in ionic conductivity from 138 to 166 mS cm<sup>-1</sup>.<sup>9</sup> However, the formation of microphase-separated structures is intricately linked to the properties of the polymer chain. When the interaction between the hydrophilic and hydrophobic components of the material is weak, the formation of microphase-separated structures becomes more challenging. Consequently, researchers have increasingly explored the use of magnetic fields<sup>10–12</sup> and electric fields<sup>13–15</sup> to induce the polymer chain segments to organize into ordered structures, thereby facilitating the creation of well-defined ion transport channels. For example, when QA-Fe<sub>3</sub>O<sub>4</sub> was doped into a TA-PPO solution under an applied magnetic field, the directional influence of the magnetic field led to the formation of ordered and fast ion transport channels in the QA-Fe<sub>3</sub>O<sub>4</sub>/TA-PPO hybrid membrane. This structural alignment resulted in a 55% increase in OH<sup>-</sup> conductivity compared to the undoped membrane.<sup>10</sup> In addition, through-plane (TP)-oriented AEMs were prepared using paramagnetic ferrocene polymers under a

Received: February 8, 2025

Revised: April 2, 2025

Accepted: April 7, 2025

Published: April 11, 2025



ACS Publications

© 2025 American Chemical Society

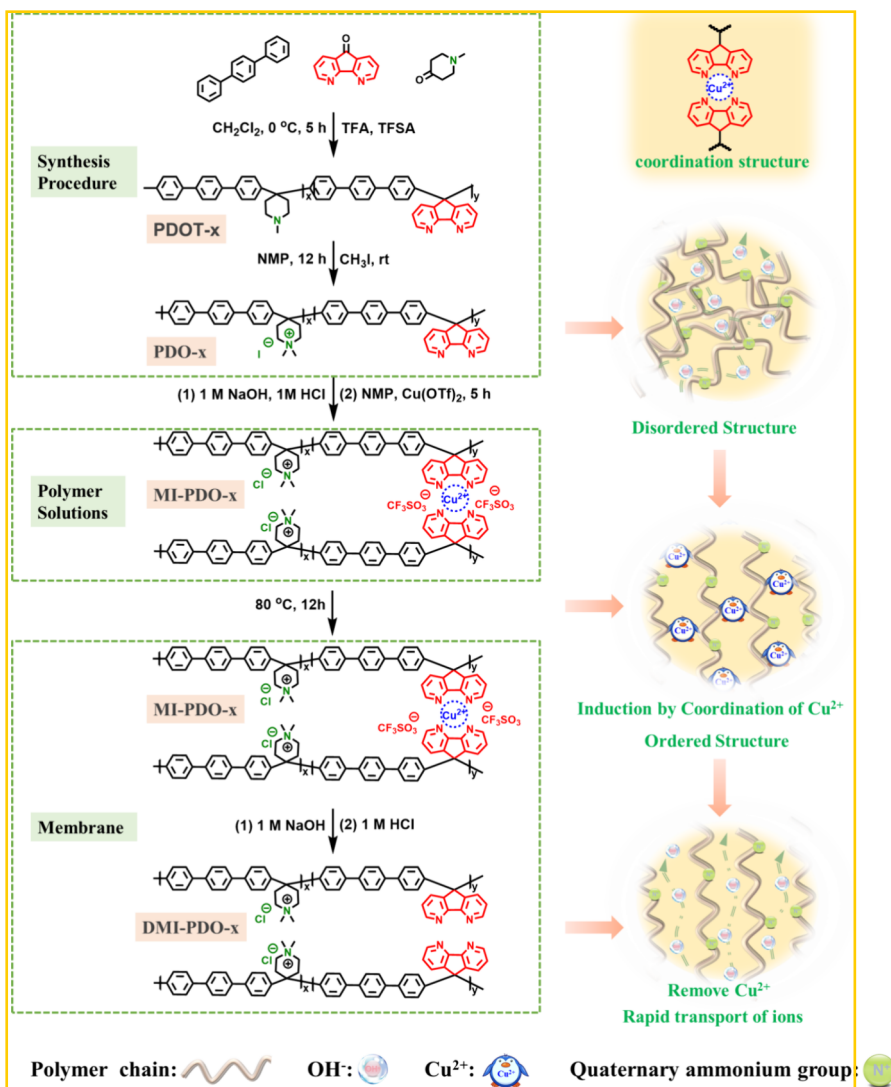


**Figure 1.** Synthetic route to PDO- $x$  and DMI-PDO- $x$ .

magnetic field, and a TP  $\text{OH}^-$  conductivity of  $\sim 160\text{ mS cm}^{-1}$  at  $95^\circ\text{C}$  was achieved.<sup>11</sup> Furthermore, utilizing the galvanic effect to induce the formation of ion transport channels along the planar direction of the AEM can also result in a substantial increase in the ionic conductivity of the LDH-containing AEM.<sup>15</sup> Although the unique approach of utilizing electric and magnetic fields to construct ion transport channels has significantly enhanced the performance of AEMs, it is important to note that these methods often rely on inorganic nanomaterials with magnetic and conductive properties. The dispersion issues associated with these materials during the membrane casting process can pose substantial risks to the performance of AEMs, making them less suitable for applications in electrochemical devices. Therefore, expanding the methods for constructing ion transport channels in homogeneous AEMs is likely to be more advantageous for the advancement of the AEM.

Based on the ideal of constructing an ordered ion channel, in this work, a series of AEMs derived from poly(diazafluorene-aryl-piperidine) were synthesized via a hyperacid-catalyzed polycondensation reaction, and then a coordination of  $\text{Cu}^{2+}$  ions with diazafluorene induced an ordered structure of the polymer chain segments within the AEMs. Subsequently, to prevent oxides formed by metal ions under alkaline conditions from

hindering ion transport,  $\text{Cu}^{2+}$  ions are removed by acid washing, thereby forming an ordered channel for fast ion transport in the membrane. The fabricated homogeneous AEMs exhibit ion channel size between 2.82 and 3.43 nm, which leads to approximately 4.7 times boosting in  $\text{OH}^-$  conductivity at most, compared to the AEMs without coordination induction. Furthermore, the AEM with ordered ion channel demonstrates impressive performance in both AEMFCs and AEMWEs.

## RESULTS AND DISCUSSION

Diazafluorene shares a configuration similar to that of the fluorene unit, except that two carbon atoms are replaced by nitrogen atoms. In coordination chemistry, diazafluorene is often considered a 2,2'-bipyridine derivative with a methylene linker connecting the two pyridine rings together. Although the overlap between the nitrogen lone pair of electrons and the metal orbitals of diazafluorene is less effective than that of 2,2'-bipyridine, it is still capable of forming weak coordination bonds with many metal ions.<sup>16–19</sup> Based on this, a series of AEMs with ordered ion transport channels derived from poly(diazafluorene-aryl-piperidine) were synthesized. In the detailed synthesis path illustrated in Figure 1, PDOT- $x$  (where  $x$  represents the molar ratio (in percent) of 4,5-diazafluoren-9-one

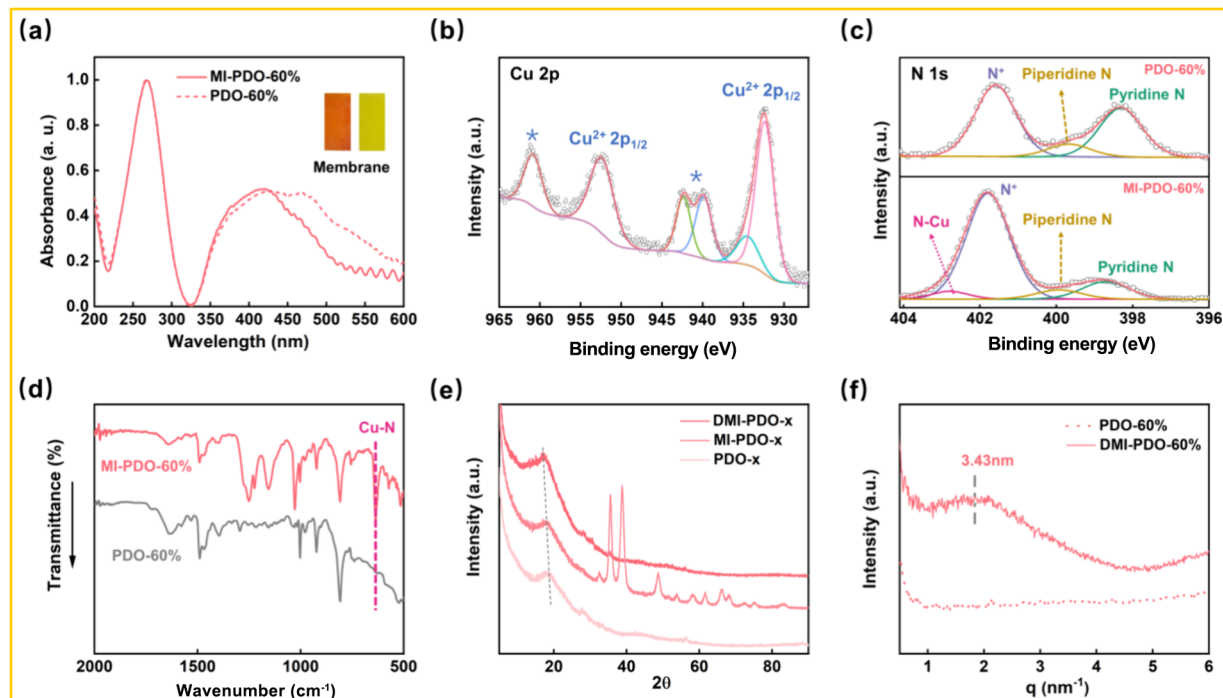


**Figure 2.** (a) UV/vis spectra of AEM; (b) XPS of Cu 2p spectrum in MI-PDO 60%; (c) XPS of N 1s spectrum in PDO 60% and MI-PDO 60%; (d) FT-IR spectra of PDO 60% and MI-PDO 60%; (e) XRD of AEM; (f) small-angle X-ray scattering (SAXS) patterns of PDO 60% and DMI-PDO 60%.

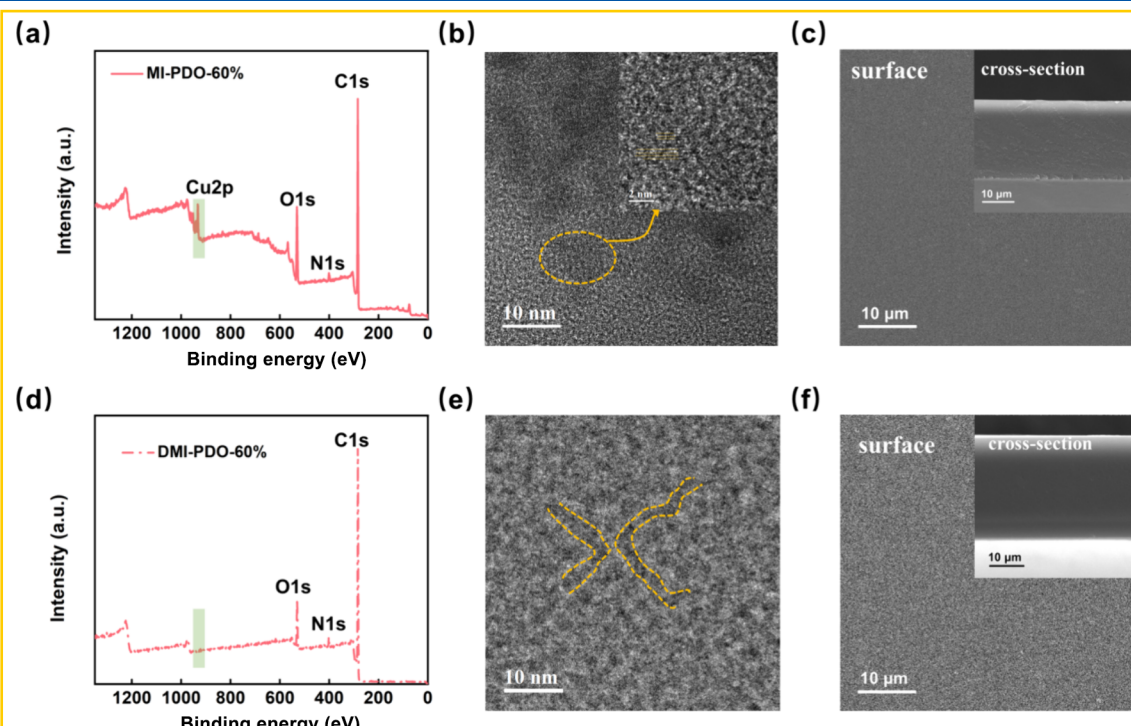


**Figure 3.** (a) Full survey XPS spectra of MI-PDO 60%; (b) HRTEM image of MI-PDO 60%; (c) surface and cross-sectional SEM image of MI-PDO-60%; (d) full survey XPS spectra of DMI-PDO 60%; (e) HRTEM image of DMI-PDO 60%; (f) surface and cross-sectional SEM images of DMI-PDO-60%.

to *p*-terphenyl) was synthesized via a trifluoromethanesulfonic acid (TFSA)-catalyzed polycondensation reaction involving *p*-terphenyl, 4,5-diazafluoren-9-one, and *N*-methyl-4-piperidone. Subsequently, PDO<sub>x</sub> membranes exhibiting disordered structures were prepared using the Menshutkin reaction of PDOT<sub>x</sub> with CH<sub>3</sub>I. Furthermore, a series of metal-coordinated MI-PDO<sub>x</sub> polymers with an ordered structure were successfully

synthesized by utilizing the coordination properties of Cu<sup>2+</sup> with the group of diazafluorene. Ultimately, the MI-PDO<sub>x</sub> membranes underwent repeated alkaline and acid washing to produce coordination-induced DMI-PDO<sub>x</sub> membranes with ordered ion transport channels. As shown in Table S1, the membrane thickness remained unchanged, indicating that the quality of the AEM was not affected during the acid-washing

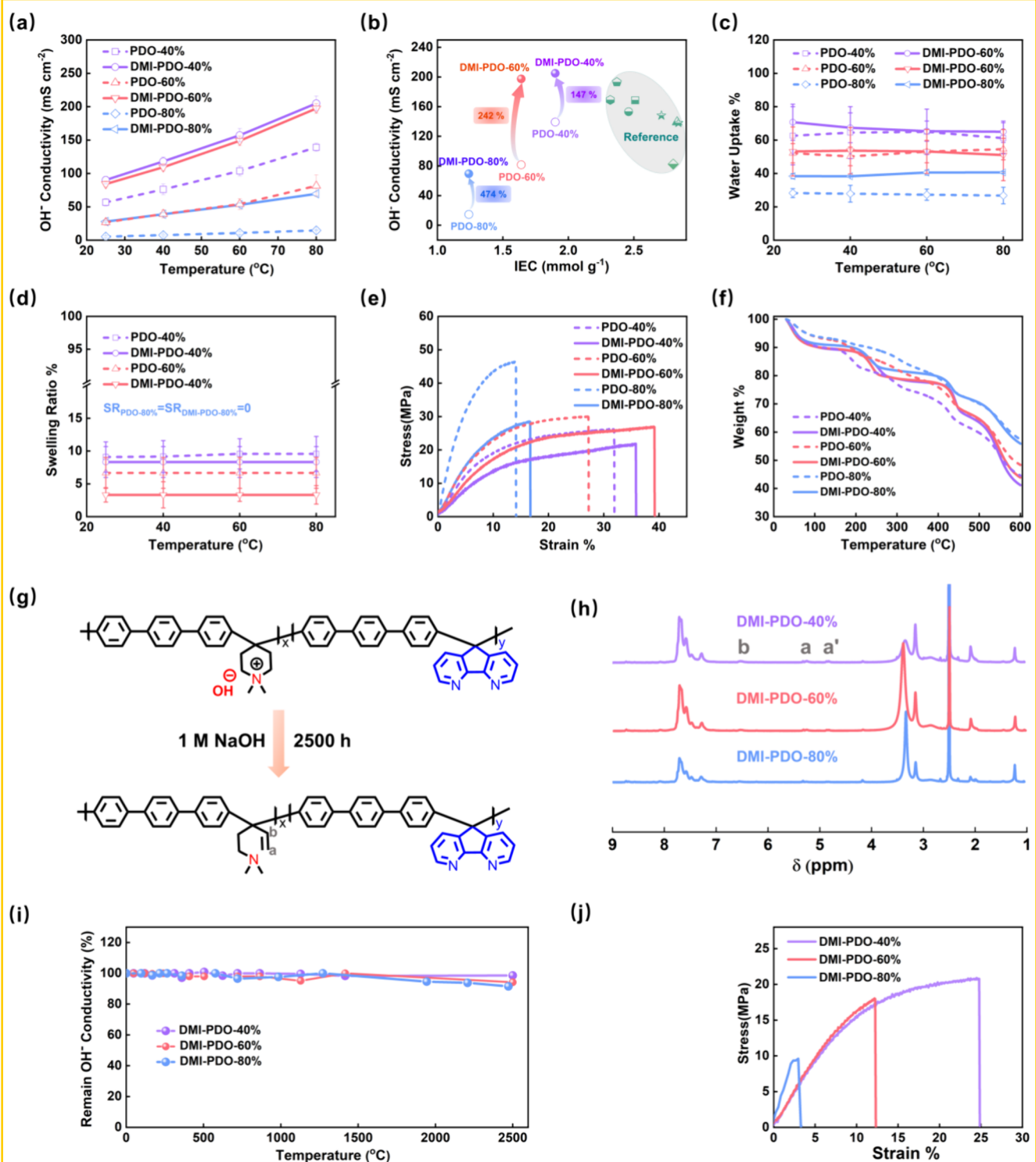


**Figure 4.** (a) OH<sup>-</sup> conductivity of AEMs at different temperatures; (b) comparison of the OH<sup>-</sup> conductivity at 80 °C and IEC of PDO and DMI-PDO with representative AEMs from other references, and the green points represent data from the references, while the various types of points indicate different sources, as detailed in Table S4; (c) water uptake and (d) swelling ratio of AEMs at different temperatures of AEMs; (e) stress-strain and (f) TGA curves of AEMs; (g) degradation mechanism of DMI-PDO; (h) <sup>1</sup>H NMR spectrum of DMI-PDO after immersion in 1 mol L<sup>-1</sup> NaOH for 2500 h at 80 °C; (i) OH<sup>-</sup> conductivity decay of DMI-PDO in 1 mol L<sup>-1</sup> NaOH for 2500 h at 80 °C; (j) mechanical properties of DMI-PDO after immersed in 1 mol L<sup>-1</sup> NaOH for 2500 h at 80 °C.

process. The photographs of various AEMs and <sup>1</sup>H NMR spectra of polymers are presented in Figures S1 and S2, respectively.

Figure 2a and Figure S3 demonstrate a comparison of the UV-vis absorption spectra of AEMs before and after

coordination with Cu<sup>2+</sup>. It was evident that the UV absorption peaks of AEMs exhibited a blue shift following coordination, with the extent of the blue shift increasing progressively with the number of ligands, primarily attributed to the Cu d-d transition.<sup>20–22</sup> The Cu and N valence and bonding states in

the AEM were analyzed using XPS. As shown in Figure 2b and Figure S4a, the Cu 2p XPS peaks at 932.3 and 952.7 eV along with the characteristic satellite peaks, confirmed the presence of Cu<sup>2+</sup> ions in the MI-PDO<sub>x</sub> membrane. Figure 2c and Figure S5 displays the N 1s XPS spectra of PDO<sub>x</sub> and MI-PDO<sub>x</sub>, with a new peak at 402.88 eV in the MI-PDO<sub>x</sub> membrane, indicating the formation of the Cu–N bond.<sup>23,24</sup> Additionally, stretching vibration peaks attributed to Cu–N at 636 cm<sup>-1</sup> also were observed in the FT-IR spectra of MI-PDO<sub>x</sub> (Figure 2d and Figure S6),<sup>25</sup> further confirming that Cu<sup>2+</sup> ions had successfully formed coordinate bonds with N. Moreover, Cu<sup>2+</sup> in AEM readily reacted with OH<sup>-</sup> under alkaline conditions, leading to the leaching of Cu<sup>2+</sup> (Cu(OH)<sub>2</sub>), followed by possible decomposing to CuO under high temperature (black particles observed). To remove the possible formed Cu(OH)<sub>2</sub> and CuO from MI-PDO<sub>x</sub>, repeated acid washing was adopted to obtain DMI-PDO<sub>x</sub>. The final membrane DMI-PDO<sub>x</sub> was characterized by Cu 2p XPS and XRD. The results are shown in Figure S4b and Figure 2e, where no Cu-related peaks were observed, which, together with the ICP-Cu in Table S2, confirmed that the Cu<sup>2+</sup> ion had been completely removed.

To investigate the effect of coordination induction on the microstructural morphology of AEMs, SAXS profiles were analyzed, as illustrated in Figure 2f and Figure S7. Compared to PDO<sub>x</sub>, DMI-PDO<sub>x</sub> exhibited a distinct scattering peak corresponding to a *d* spacing of 2.82–3.43 nm, indicating that coordination induction facilitated the formation of a well-defined ion transport channel within the AEM. This result was consistent with that observed by TEM. First, under the influence of coordination with Cu<sup>2+</sup> ions, a Cu 2p peak appeared in the XPS total spectrum of MI-PDO<sub>x</sub> (Figure 3a and Figure S8), while a weak metal lattice streak was also shown in MI-PDO-60% (Figure 3b), but these did not affect the dense structure of the AEM (Figure 3c). Subsequently, the peak corresponding to Cu was absent in the XPS total spectrum (Figure 3d) following the removal of Cu<sup>2+</sup> ions, further confirming that DMI-PDO<sub>x</sub> had been thoroughly washed. Figure 3e shows the TEM image of DMI-PDO-60% with the bright areas representing hydrophobic structural domains and the dark areas representing hydrophilic structural domains, where well-connected and ordered ion-transport channels were observed (yellow curve). Combined with the separation of hydrophobic and hydrophilic phase domains observed in the AFM phase images (Figure S9), these findings indicate that constructing ion transport channels through coordination induction is an effective approach. Finally, to investigate the effect of washing on the compactness of the AEM, SEM was conducted on both the surface and the cross-section of the AEM, with results presented in Figure 3f and Figures S10 and S11. The observations revealed that the surface of the AEM was flat, while the cross section was dense and nonporous, which was advantageous for its application in electrochemical scenarios.

**Membrane Properties.** The ionic conductivity of AEMs is a crucial factor influencing the performance of AEMFCs and AEMWEs. To investigate the impact of coordination induction on ionic conductivity, the OH<sup>-</sup> conductivity of AEMs was measured before and after coordination induction at various temperatures. As shown in Figure 4a, similar to that of traditional AEMs, the OH<sup>-</sup> conductivity of AEMs exhibited a positive correlation with temperature. The OH<sup>-</sup> conductivity of each series of AEMs showed a strong dependence on the IEC, with PDO 40% and DMI-PDO 40%, which possessed the highest IEC (1.90 mmol g<sup>-1</sup> Table S3), demonstrating optimal

OH<sup>-</sup> conductivity in the PDO<sub>x</sub> and DMI-PDO<sub>x</sub> series, respectively. Notably, a significant enhancement in the conductivity of AEMs was observed after coordination induction. Specifically, DMI-PDO 40%, DMI-PDO 60%, and DMI-PDO 80% exhibited OH<sup>-</sup> conductivities of 90, 84, and 27 mS cm<sup>-1</sup> at 25 °C, respectively. In contrast, the OH<sup>-</sup> conductivities of PDO 40%, PDO 60%, and PDO-80% were only 57, 27, and 5 mS cm<sup>-1</sup> at 25 °C, respectively. This variation in the OH<sup>-</sup> conductivity was primarily attributed to the coordination induction that facilitated the formation of ordered ion transport channels. Moreover, the degree of conductivity enhancement in DMI-PDO<sub>x</sub> varied with the content of 4,5-diazafluoren-9-one, with DMI-PDO 80% showing the most significant enhancement—4.7 times than that of PDO 80% (Figure 4b). This was because 4,5-diazafluoren-9-one was the ligand and played a decisive role in the formation of ordered ion transport channels. Under the influence of the ordered ion channels formed by coordination induction, the AEM prepared in this work possessed a superior conductivity than the AEM in the literature at low IEC (Table S4).<sup>3,5,6,8,9,26,27</sup>

Although high water uptake is generally beneficial for high OH<sup>-</sup> conductivity, excessive water uptake can lead to over membrane swelling and eventual fragmentation of the AEM. Therefore, it is desirable to develop AEMs with excellent OH<sup>-</sup> conductivity without excessive water uptake. In this study, the water uptakes and swelling ratios of DMI-PDO<sub>x</sub> and PDO<sub>x</sub> were compared, as depicted in Figure 4c,d. Unsurprisingly, for both PDO<sub>x</sub> and DMI-PDO<sub>x</sub>, the water uptake and swelling ratio showed an increasing trend with increasing IEC. Additionally, following the removal of Cu<sup>2+</sup>, "microvacancies" form in DMI-PDO<sub>x</sub>, leading to an increase in free volume that facilitates the ingress of water molecules into the AEM, resulting in the WU of DMI-PDO<sub>x</sub> being slightly higher than that of PDO<sub>x</sub>. However, the swelling ratio was slightly lower than that of PDO<sub>x</sub>, which may be due to the coordination interactions enhancing the ordered stacking of the polymer segments. This compact AEM structure, to some extent, hinders the swelling of the AEM. However, it was noteworthy that the AEM exhibited less than a 10% swelling ratio in the 28 and 71% water uptake intervals, which was highly beneficial for maintaining the mechanical properties of fully hydrated AEMs.

The mechanical properties of the AEMs are shown in Figure 4e. It was evident that the overall tensile stress of the AEMs decreased while the strain increased, following coordination induction. This trend was closely related to the WU of the membranes, as water generally acted as a plasticizer, enhancing the toughness of the AEM. Furthermore, it was noteworthy that the tensile stresses of all AEMs exceed 20 MPa, which was attributed to the benefits of the all-aromatic structure of the AEM. The thermal decomposition temperature of the AEMs was evaluated using TGA under a N<sub>2</sub> atmosphere (Figure 4f). As can be seen, the decomposition of the AEMs occurred in three distinct steps. The weight loss in the first step, occurring before 100 °C, most probably corresponded to the evaporation of water. Subsequently, the second step of weight loss, observed around 200 °C, was indicative of the degradation and loss of the piperidine cation. Finally, the backbone of the AEM decomposed at approximately 400 °C. The high decomposition temperature of the AEM suggested that the AEMs were suitable for both AEMFC and AEMWE.

To assess the alkaline stability of the AEMs, DMI-PDO<sub>x</sub> and PDO<sub>x</sub> were immersed in a 1 mol L<sup>-1</sup> NaOH aqueous solution at 80 °C for ex situ testing. After 2500 h of testing, the membrane

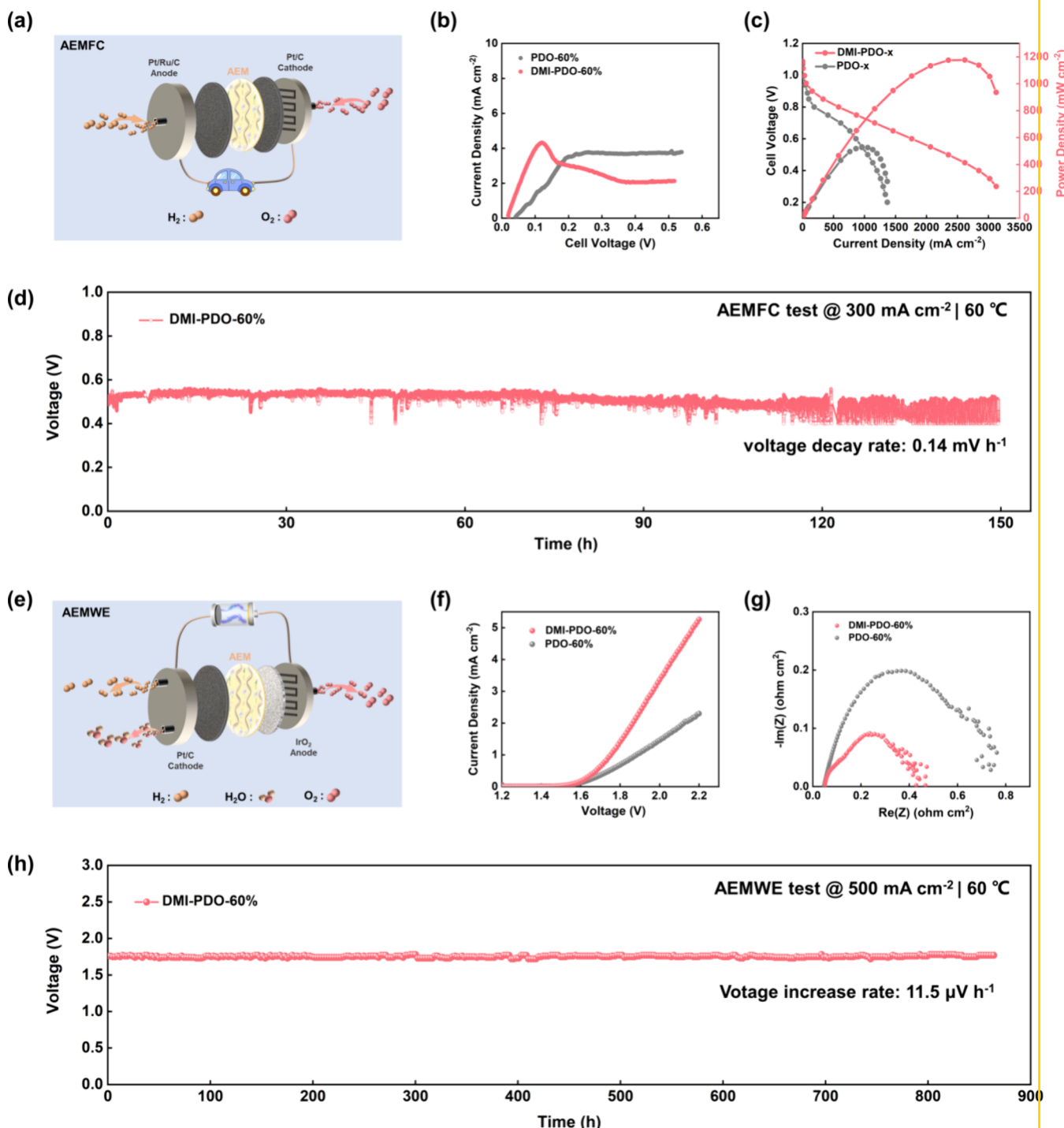


**Figure 5.** (a) Schematic of AEMFC cell; (b) LSV of MEAs based on PDO-x and DMI-PDO-60% testing conditions [100%/100% A/C RH,  $80^\circ\text{C}$ ,  $1 \text{ mV s}^{-1}$ , and free-backpressure]; (c) AEMFC performance based on PDO-60% and DMI-PDO-60% at  $80^\circ\text{C}$ ; (d) in situ durability performance of AEMFC with DMI-PDO-60% based MEA at  $60^\circ\text{C}$  under a current density of  $300 \text{ mA cm}^{-2}$  and without backpressure; (e) schematic of AEMWE cell; (f) polarization curves at the temperature of  $80^\circ\text{C}$  Catalyst loadings were  $2.0 \text{ mg IrO}_2 \text{ cm}^{-2}$  at the anode and  $1 \text{ mg Pt cm}^{-2}$  at the cathode; (g) Nyquist plots at the operating temperature of  $80^\circ\text{C}$ ; (h) long-term stability performance of AEMWE at  $500 \text{ mA cm}^{-2}$  and  $60^\circ\text{C}$  in  $1 \text{ mol L}^{-1} \text{ NaOH}$ .

remained intact, showing no visible cracks or holes. However, SAXS measurements indicated a slight reduction in the size of the ion channels in DMI-PDO-40% and DMI-PDO-60% (Figure S12), which may be attributed to excessive water absorption disrupting the segmental order. In contrast, the ion channel size in DMI-PDO-80%, which exhibited low water absorption, showed almost no change. Additionally, the piperidine ring, as a potential degradation pathway for anion

exchange membranes (AEMs), is also susceptible to  $\text{OH}^-$  attack (Figure 4g and Figure S13a). To investigate the potential degradation reactions, the  $^1\text{H}$  NMR spectra of the AEMs were analyzed after exposure to alkali resistance, and the results were shown in Figure 4h and Figure S13b. Not surprisingly, new peaks attributed to  $\text{C}=\text{C}$  protons appeared at chemical shifts of 6.52 (at position b), 5.26 (at position a), and 4.84 ppm (at position a') compared to the  $^1\text{H}$  NMR spectra before alkali

resistance. Based on this result, a corresponding decrease in conductivity was observed for both DMI-PDO<sub>x</sub> and PDO<sub>x</sub>. Specifically, among the DMI-PDO<sub>x</sub> series (Figure 4*i*), DMI-PDO-80% exhibited the highest degradation of 9.24%, while the degradation for DMI-PDO-40% and DMI-PDO-60% were 1.44% and 8.46%, respectively. This was primarily because the maximum water uptake of DMI-PDO-40% effectively diluted the OH<sup>-</sup> concentration around the piperidine ring, thereby reducing the nucleophilicity and basicity of OH<sup>-</sup>.<sup>28,29</sup> Similarly, the degradation of PDO<sub>x</sub> followed a comparable trend to DMI-PDO<sub>x</sub> (Figure S13c), with PDO-80% showing the highest degradation at 16.77% followed by PDO-60% (11.74%) and PDO-40% (4.47%). However, all of these data were significantly higher than those of the DMI-PDO<sub>x</sub> series. This was attributed to the ordered structure in DMI-PDO<sub>x</sub>, which promoted the formation of ionic clusters, leading to the accumulation of water and a reduction in OH<sup>-</sup> concentration around the functional groups. Figure 4*j* and Figure S13d depict the mechanical properties of the AEMs after 2500 h in a 1 mol L<sup>-1</sup> NaOH solution. At lower levels of water uptake, AEMs tended to exhibit increased brittleness but were still able to maintain mechanical properties in excess of 5 MPa.

The fuel cell performances with different AEMs were evaluated at 80 °C with 100% relative humidity at both the anode and cathode sides using H<sub>2</sub>-O<sub>2</sub> (Figure 5a). It is seen in Figure 5b that the hydrogen permeation current of DMI-PDO-60% was lower than that of PDO-60%. This indicated that the AEM maintained good gas tightness even after Cu<sup>2+</sup> ion removal. Figure S14 demonstrates the trend of H<sub>2</sub>-O<sub>2</sub> fuel cell power density with increasing backpressure for DMI-PDO-60% based-MEA. Consistent with other fuel cells, increasing the backpressure proved to be beneficial. Specifically, the peak power density increased from 0.7 to 1.1 W cm<sup>-2</sup> as the backpressure was increased from 0 to 0.1 MPa. The maximum peak power density of 1.2 W cm<sup>-2</sup> was achieved at 0.45 V at a backpressure of 0.2 MPa. In contrast, the PDO-60% based-AEM fuel cell reached only a peak power density of 0.53 W cm<sup>-2</sup> at 80 °C and 0.2 MPa backpressure (Figure 5c), which was only 44% of that achieved by the DMI-PDO-60%. Finally, the DMI-PDO-60% AEM-based fuel cell was further subjected to in situ durability testing at a constant current density of 0.3 A cm<sup>-2</sup> at 60 °C and the results were shown in Figure 5d. The voltage decay rate of the DMI-PDO-60%-based MEA was 0.14 mV h<sup>-1</sup> after 150 h.

In addition to AEMFC, the AEMWE performance of the DMI-PDO-60% and PDO-60% membranes was evaluated. The *i*-V curves at different temperatures were measured in 1 mol L<sup>-1</sup> NaOH using 2 mg cm<sup>-2</sup> IrO<sub>x</sub> and 1 mg cm<sup>-2</sup> Pt/C as the anode and cathode catalysts, respectively (Figure 5e). The MEA was assembled by using a conventional catalyst-coated substrate (CCS) method. At the operating temperature of 80 °C, the current density of the DMI-PDO-60%-based cell at 2.0 V was 3.4 A cm<sup>-2</sup> while the PDO-60% based cell was only 1.5 A cm<sup>-2</sup> (Figure 5f). The lower performance of the PDO-60% based cell may be due to the poor OH<sup>-</sup> transfer efficiency of PDO-60% relative to DMI-PDO-60%, which was evidenced by the lower ohmic resistance (Rohm) of DMI-PDO-60%-based MEA relative to that of PDO-60%-based MEA (Figure 5g). Finally, the PDO-60% based MEA and DMI-PDO-60%-based MEA were tested for electrolytic water stability, respectively, and the results are shown in Figure 5h. The voltage increase rate of the DMI-PDO-60%-based MEA was 11.5 μV h<sup>-1</sup> after continuous

electrolysis for 864 h at a current density of 500 mA cm<sup>-2</sup> in a 1 mol L<sup>-1</sup> NaOH solution at 60 °C.

## CONCLUSIONS

In summary, this study employed a novel method to construct ordered ion transport channels by coordination induction within the AEM of DMI-PDO<sub>x</sub>. The coordination of Cu<sup>2+</sup> ions with diazafluorene induced an ordered structure of the polymer chain segments within the AEMs, thereby forming an ordered channel for fast ion transport in the membrane after the removal of Cu<sup>2+</sup> ions. The fabricated AEMs exhibited ion channel size between 2.82 and 3.43 nm, which improved the ion transfer properties of the DMI-PDO<sub>x</sub> membrane. Consequently, the DMI-PDO<sub>x</sub> membrane achieved OH<sup>-</sup> conductivities that were 4.7 times greater than those of the PDO<sub>x</sub> membrane, which did not utilize coordination induction. Furthermore, the DMI-PDO<sub>x</sub> membrane maintained over 98% of its OH<sup>-</sup> conductivity after 2500 h in 1 mol L<sup>-1</sup> NaOH solution at 80 °C. Additionally, the DMI-PDO-60%-based MEA reached a peak power density of 1.2 W cm<sup>-2</sup> in an AEMFC, and it had a voltage decay rate of only 0.14 mV h<sup>-1</sup> after 150 h at a current density of 300 mA cm<sup>-2</sup>. The DMI-PDO-60%-based MEA also demonstrated superior performance compared with the PDO-60%-based MEA in an AEMWE, achieving a current density of 3.4 A cm<sup>-2</sup> at 2 V. Moreover, it exhibited a voltage decay rate of only 11.5 μV h<sup>-1</sup> over 864 h of continuous electrolytic operation at a current density of 500 mA cm<sup>-2</sup> at 60 °C in a 1 mol L<sup>-1</sup> NaOH solution.

## ASSOCIATED CONTENT

### Supporting Information

The Supporting Information is available free of charge at <https://pubs.acs.org/doi/10.1021/acs.macromol.Sc00353>.

Materials and measurements; syntheses of polymer precursors; photographs of AEM; <sup>1</sup>H NMR spectra polymers; UV-vis spectrum, XPS spectrum, FT-IR spectrum, small-angle X-ray scattering patterns, SEM images of AEM; IEC, WU, SR, OH<sup>-</sup> conductivity, stress and strain of AEMs; degradation mechanism of PDO<sub>x</sub>; AEMFC performance based on DMI-PDO-60%; and comparisons of AEM in this work and reference data (PDF)

## AUTHOR INFORMATION

### Corresponding Authors

Jianchuan Wang – School of Chemistry and Chemical Engineering, State Key Laboratory of Advanced Chemical Power Sources, Chongqing University, Chongqing 400044, China; [orcid.org/0000-0002-4632-9413](https://orcid.org/0000-0002-4632-9413); Email: jxw319@cqu.edu.cn

Zidong Wei – School of Chemistry and Chemical Engineering, State Key Laboratory of Advanced Chemical Power Sources, Chongqing University, Chongqing 400044, China; [orcid.org/0000-0001-8001-9729](https://orcid.org/0000-0001-8001-9729); Email: zdwei@cqu.edu.cn

### Authors

Caili Yuan – School of Chemistry and Chemical Engineering, State Key Laboratory of Advanced Chemical Power Sources, Chongqing University, Chongqing 400044, China

Yuhang Chen – School of Chemistry and Chemical Engineering, State Key Laboratory of Advanced Chemical Power Sources, Chongqing University, Chongqing 400044, China

Xiaoqin Ma — School of Chemistry and Chemical Engineering,  
State Key Laboratory of Advanced Chemical Power Sources,  
Chongqing University, Chongqing 400044, China

Xiaoli Lu — School of Chemistry and Chemical Engineering,  
State Key Laboratory of Advanced Chemical Power Sources,  
Chongqing University, Chongqing 400044, China

Wei Yuan — School of Chemistry and Chemical Engineering,  
State Key Laboratory of Advanced Chemical Power Sources,  
Chongqing University, Chongqing 400044, China

Complete contact information is available at:

<https://pubs.acs.org/10.1021/acs.macromol.5c00353>

## Author Contributions

The manuscript was written through contributions of all authors. All authors have given approval to the final version of the manuscript.

## Notes

The authors declare no competing financial interest.

## ACKNOWLEDGMENTS

The authors would like to express great thanks to the financial support of the National Key Research and Development Program of China (2021YFB4001200) and the Natural Science Foundation of China (grant no. 22478044).

## REFERENCES

- (1) Zheng, W.; He, L.; Tang, T.; Rong, R.; Lee, H.; Ding, G.; Wang, L.; Sun, L. Poly(Dibenzothiophene-Terphenyl Piperidinium) for High-performance Anion Exchange Membrane Water Electrolysis. *Angew. Chem., Int. Ed.* 2024, 136 (34), No. e202405738.
- (2) Wan, L.; Liu, J.; Lin, D.; Xu, Z.; Chen, Y.; Pang, M.; Xu, Q.; Wang, B. 3D-ordered catalytic nanoarrays interlocked on anion exchange membranes for water electrolysis. *Energy Environ. Sci.* 2024, 17 (10), 3396–3408.
- (3) Kim, S.; Yang, S. H.; Shin, S.-H.; Cho, H. J.; Jang, J. K.; Kim, T. H.; Oh, S.-G.; Kim, T.-H.; Han, H.; Lee, J. Y. High-performance and durable anion-exchange membrane water electrolyzers with high-molecular-weight polycarbazole-based anion-conducting polymer. *Energy Environ. Sci.* 2024, 17 (15), 5399–5409.
- (4) Du, W.; Liu, L.; Yin, L.; Li, B.; Ma, Y.; Guo, X.; Zang, H. Y.; Zhang, N.; Zhu, G. Ultrathin Free-Standing Porous Aromatic Framework Membranes for Efficient Anion Transport. *Angew. Chem., Int. Ed.* 2024, 63 (22), No. e202402943.
- (5) Zeng, M.; He, X.; Wen, J.; Zhang, G.; Zhang, H.; Feng, H.; Qian, Y.; Li, M. N-Methylquinuclidinium-Based Anion Exchange Membrane with Ultrahigh Alkaline Stability. *Adv. Mater.* 2023, 35 (51), No. 2306675.
- (6) Wang, J.; Zhao, Y.; Setzler, B. P.; Rojas-Carbonell, S.; Ben Yehuda, C.; Amel, A.; Page, M.; Wang, L.; Hu, K.; Shi, L.; Gottesfeld, S.; Xu, B.; Yan, Y. Poly(aryl piperidinium) membranes and ionomers for hydroxide exchange membrane fuel cells. *Nat. Energy* 2019, 4 (5), 397–398.
- (7) Zhu, L.; Yu, X.; Peng, X.; Zimudzi, T. J.; Saikia, N.; Kwasny, M. T.; Song, S.; Kushner, D. I.; Fu, Z.; Tew, G. N.; Mustain, W. E.; Yandrasits, M. A.; Hickner, M. A. Poly(olefin)-Based Anion Exchange Membranes Prepared Using Ziegler–Natta Polymerization. *Macromolecules* 2019, 52 (11), 4030–4041.
- (8) Xu, G.; Pan, J.; Zou, X.; Jin, Z.; Zhang, J.; Fang, P.; Zhang, Q.; Sun, Z.; Yan, F. High-performance Poly(biphenyl piperidinium) Type Anion Exchange Membranes with Interconnected Ion Transfer Channels: Cooperativity of Dual Cations and Fluorinated Side Chains. *Adv. Funct. Mater.* 2023, 33 (35), No. 2302364.
- (9) Wu, X.; Chen, N.; Hu, C.; Klok, H. A.; Lee, Y. M.; Hu, X. Fluorinated Poly(Aryl Piperidinium) Membranes for Anion Exchange Membrane Fuel Cells. *Adv. Mater.* 2023, 35 (26), No. e2210432.
- (10) Chen, N.; Wang, D.; Long, C.; Li, Y.; Lu, C.; Wang, F.; Zhu, H. Magnetic field-oriented ferroferric oxide/poly(2,6-dimethyl-1,4-phenylene oxide) hybrid membranes for anion exchange membrane applications. *Nanoscale* 2018, 10 (39), 18680–18689.
- (11) Liu, X.; Xie, N.; Xue, J.; Li, M.; Zheng, C.; Zhang, J.; Qin, Y.; Yin, Y.; Dekel, D. R.; Guiver, M. D. Magnetic-field-oriented mixed-valence-stabilized ferrocenium anion-exchange membranes for fuel cells. *Nat. Energy* 2022, 7 (4), 329–339.
- (12) Yang, H.; Ma, X.; Ma, W.; Shi, M.; Zhang, J.; Jiang, Y.; Cao, Z.; Gong, F.; Pan, J. Magnetic field-assisted widened short-range ion channels to facilitate ion conductivity for alkaline anion exchange membrane fuel cell. *J. Membr. Sci.* 2025, 771, No. 123600.
- (13) Kim, J.-H.; Ryu, S.; Lee, J.-Y.; Moon, S.-H. Preparation of high-conductivity QPPO (quaternary-amino poly (2,6-dimethyl-1,4-phenyleneoxide)) membranes by electrical treatment. *J. Membr. Sci.* 2018, 553, 82–89.
- (14) Zhu, H.; Li, R.; Chen, N.; Wang, F.; Wang, Z.; Han, K. Electrorheological effect induced quaternized poly(2,6-dimethyl phenylene oxide)-layered double hydroxide composite membranes for anion exchange membrane fuel cells. *RSC Adv.* 2016, 6 (88), 85486–85494.
- (15) Fan, J.; Zhu, H.; Li, R.; Chen, N.; Han, K. Layered double hydroxide-polyphosphazene-based ionomer hybrid membranes with electric field-aligned domains for hydroxide transport. *Journal of Materials Chemistry A* 2014, 2 (22), 8376.
- (16) Annibale, V. T.; Song, D. Coordination chemistry and applications of versatile 4,5-diazafluorene derivatives. *Dalton Transactions* 2016, 45 (1), 32–49.
- (17) Wong, K.-T.; Chen, H.-F.; Fang, F.-C. Novel Spiro-Configured PET Chromophores Incorporating 4,5-Diazafluorene Moiety as an Electron Acceptor. *Org. Lett.* 2006, 8 (16), 3501–3504.
- (18) Li, W.-J.; Liu, B.; Qian, Y.; Xie, L.-H.; Wang, J.; Li, S.-B.; Huang, W. Synthesis and characterization of diazafluorene-based oligofluorenes and polyfluorene. *Polym. Chem.* 2013, 4 (6), 1796.
- (19) Baysal, A.; Connor, J. A.; Wallis, J. D. Complexes of 4,5-Diazafluorene and 9,9'-Bis(4,5-Diazafluorenyl) with Nickel(II), Copper(II) and Zinc(II). *J. Coord. Chem.* 2001, 53 (4), 347–354.
- (20) Krockert, K. W.; Garg, F.; Heck, J.; Heinz, M. V.; Lange, J.; Schmidt, K.; Hoffmann, A.; Herres-Pawlis, S. ATRP catalysts of tetradeятate guanidine ligands – do guanidine donors induce a faster atom transfer? *Dalton Transactions* 2024, 53 (7), 2973–2990.
- (21) Li, Y.; Fan, W.; Zhang, Z.; Xie, X.; Xiang, S.; Huang, D. Copper(II)-hydroxide facilitated C–C bond formation: the carboxyamido pyridine system versus the methylimino pyridine system. *Dalton Transactions* 2020, 49 (35), 12189–12196.
- (22) Kirin, S. I.; Dübon, P.; Weyhermüller, T.; Bill, E.; Metzler-Nolte, N. Amino Acid and Peptide Bioconjugates of Copper(II) and Zinc(II) Complexes with a Modified N,N-Bis(2-picoly)amine Ligand. *Inorg. Chem.* 2005, 44 (15), 5405–5415.
- (23) Wu, M.; Zhang, X.; Zhao, Y.; Yang, C.; Jing, S.; Wu, Q.; Brozena, A.; Miller, J. T.; Libretto, N. J.; Wu, T.; Bhattacharyya, S.; Garaga, M. N.; Zhang, Y.; Qi, Y.; Greenbaum, S. G.; Briber, R. M.; Yan, Y.; Hu, L. A high-performance hydroxide exchange membrane enabled by Cu<sup>2+</sup>-crosslinked chitosan. *Nat. Nanotechnol.* 2022, 17 (6), 629–636.
- (24) Zhao, X.; Chen, J.; Mao, X.; Li, C.; He, J.; Zhang, F.; Zhang, M.; Diwu, J.; Wu, G.; Chai, Z.; Wang, S. One-Pot Synthesis of a Mixed-Valent Copper(I/II)-Coordinated Covalent Organic Framework Induced by  $\gamma$ -Ray Radiation. *Inorg. Chem.* 2024, 63 (26), 12333–12341.
- (25) Gashu, M.; Aragaw, B. A.; Tefera, M.; Abebe, A. Poly(bis[2,2-bipyridine]) hydroxy Copper(II) iodide modified glassy carbon electrode for electrochemical determination of chloroquine in pharmaceuticals and biological samples. *Sensing and Bio-Sensing Research* 2023, 42, No. 100598.
- (26) Hu, C.; Park, J. H.; Kang, N. Y.; Zhang, X.; Lee, Y. J.; Jeong, S. W.; Lee, Y. M. Effects of hydrophobic side chains in poly(fluorenyl-co-aryl piperidinium) ionomers for durable anion exchange membrane fuel cells. *J. Mater. Chem. A* 2023, 11 (4), 2031–2041.

- (27) Allushi, A.; Bakvand, P. M.; Jannasch, P. Polyfluorenes Bearing N,N-Dimethylpiperidinium Cations on Short Spacers for Durable Anion Exchange Membranes. *Macromolecules* 2023, 56 (3), 1165–1176.
- (28) Willdorf-Cohen, S.; Zhegur-Khais, A.; Ponce-González, J.; Bsoul-Haj, S.; Varcoe, J. R.; Diesendruck, C. E.; Dekel, D. R. Alkaline Stability of Anion-Exchange Membranes. *ACS Applied Energy Materials* 2023, 6 (2), 1085–1092.
- (29) Muller, J.; Zhegur, A.; Krewer, U.; Varcoe, J. R.; Dekel, D. R. Practical ex-Situ Technique To Measure the Chemical Stability of Anion-Exchange Membranes under Conditions Simulating the Fuel Cell Environment. *ACS Mater. Lett.* 2020, 2 (2), 168–173.